Meso-Scale Nanofibrillar Organization in Spider's Orb-Web Radial Fibers

Christian Riekel, Tilman A Grünewald

To cite this version:

Christian Riekel, Tilman A Grünewald. Meso-Scale Nanofibrillar Organization in Spider's Orb-Web Radial Fibers. Advanced Functional Materials, 2025, 35 (15), ⟨10.1002/adfm.202419631⟩. ⟨hal-05224095⟩

HAL Id: hal-05224095

https://hal.science/hal-05224095v1

Submitted on 26 Aug 2025

Meso-scale nanofibrillar organization in spider's orb-web radial fibers

Christian RIEKEL[1*] and *Tilman A. GRÜNEWALD*[2]

[1] The European Synchrotron (ESRF), 71 Avenue des Martyrs, CS40220, 38043 Grenoble Cedex 9, France

[2] Aix Marseille Univ, CNRS, Centrale Med, Institut Fresnel, Marseille, France.

[*]**Author for correspondance**
Christian RIEKEL
The European Synchrotron (ESRF), 71 Avenue des Martyrs, CS40220, 38043 Grenoble Cedex 9, France
Email: riekel@esrf.fr
Tel : +33-4-76-88-2051

Keywords: spider's orb-web, radial fibers, meso-scale order, nanofibrillar bundles, meso-scale order, synchrotron radiation scattering, X-ray nanodiffraction

ABSTRACT

Spider's orb-webs radial fibers absorb most of the impact energy of flying insects. The blend of extensibility, toughness and strength of these dragline-type fibers relies on structural proteins, called spidroins. The fibers hierarchical structural organization is attributed to crystalline β-sheet nanodomains, assembling with less-ordered protein chains into nanofibrils. Here we show that radial fibers develop structured core-surface and core-core interfaces upon bending deformation, based on assembly of nanofibrils into bundles. The bundles at the core-surface interface show meso-scale diameters. Their short length appears to be due to interactions of spidroin nanofibrils with surface proteins. Meso-scale diameter bundles at the core-core interface are, however, of extended length, coexisting with ordered domains of nanofibrillar clusters. Modeling supports an intermediary assembly level of nanofibrils clusters, composed of a central nanofibril surrounded by a shell of six nanofibrils.

1. Introduction

Spider orb-webs are optimized for absorbing the kinetic energy of flying insects upon impact[1,2]. The cores of radial (dragline-type) silk fibers, providing the major contribution to energy dissipation during impact deformation, are composed of spidroin proteins such MaSp1, MaSp2 and others, produced by the major ampullate glands[3]. Molecular dynamics (MD) simulation of MaSp1/MaSp2 molecules secondary structure reveals ordered β-sheet cores, capped by disordered chain domains[4]. X-ray diffraction (XRD) of dragline-type fibers suggests 10-15 % crystallinity based on few nm dimension crystalline particles (called here "nanodomains") within a disordered protein chain matrix[5,6]. The nanodomains lattice is assumed corresponding to the β poly(L-alanine) structure, based on pleated β-sheets (Figure S2) with the inter-sheet distance determined by side-group packing. Lamellar peaks observed by small-angle X-ray scattering (SAXS) were attributed to cylindrical nanofibrils of 6-7 nm diameter with periodic density modulation[7,8]. In analogy to synthetic polymers, the density modulation can be related to assembly of monomer units into a chain. Indeed, spidroins secondary structure[4] allows hydrogen-bonding interactions between disordered domains of neighboring monomer units[9] (Figure 4a). MD simulations suggest that lamellar morphology and crystallinity[10] as well as meso-scale (≥ 50 nm) geometric confinement[11] are at the origin of dragline-type fiber's blend of strength and toughness. Meso-scale features have, however, as yet only been observed for structurally similar bagworm silk, surpassing toughness and strength of dragline-type fibers while showing optimized crystallinity of ~ 40 % combined with exceptionally regular lamellar order[12]. Meso-scale nanofibrillar bundles were found to be particularly well developed at the interface of fibroin core with sericin surface-layer[9]. This could act as barrier for fracture propagation into the bulk, enhancing fibers toughness[9]. Bagworm silk is based on a single "heavy-chain" fibroin molecule and used in more "static" applications such as nest protection or as lifeline for dangling[12] while multi-spidroin dragline-type silk fibers are used (amongst others) for absorbing the shock of prey impacting an orb-web.

Here we are interested exploring whether these functional differences are reflected at the level of local meso-scale order without disrupting fragile interfaces. Indeed, probing longitudinal bagworm sections allows avoiding strong scattering from the sericin surface layer but introduces artifacts at the interface due to embedding procedures[9]. Dragline-type fiber's spidroin core is also covered by several, albeit thinner, surface-layers including a protein and glycoprotein layer[13]. An impact of embedding on the core's hierarchical organization can also not be excluded. Here we apply bending stress to radial fibers for enhancing nanofibrillar assembly at the core interface. Excessive bending stress has, however, to be avoided as MD simulations reveal the appearance of shear- or crack-like nanodomains failure processes, which could mask meso-scale scattering[14]. We will show that limiting bending into an arc of few hundred μm radius allows preserving the nanodomains orientation distribution across the fiber.

We probed a radial-type anchor (also called "bridge") thread[15] collected from the orb-web of an *Argiope bruennichi* spider in its natural habitat[8], avoiding artifacts associated with forced silking techniques[16]. Sections of the thread were bent into an arc or knot and glued to a Si_3N_4 support (Figure S1a-c). Scanning nanobeam XRD (nanoXRD) was performed in transmission geometry[8] with the beam direction normal to the loading direction. Details on the experimental setup are provided in the *Supporting Information.*

2. Results and Simulations

2.1. Crystallography of bent and unbent fibers

An optical image of a thread, bent to a radius of r_b~231 μm, is shown in Figure 1a. The superimposed composite density map (DM)[8] obtained from a mesh-scan is based on pixels covering only the area of the (020)/(210) Bragg peaks from each recorded 2D pattern. The homogeneous density distribution reveals superposition of the two fibers in the thread while DMs for the unbent thread were obtained from two parallel fibers (Figure S8a-9). Averaging patterns recorded at 81 mesh-points for the unbent thread shows reflections of the nanodomains β-poly(L-alanine) type lattice[8,17] and the strongest polyglycine II (100) reflection from the semicrystalline glycoprotein skin-layer[18,19] (Figure 1b). The nanodomains, with up to ~10^8 unit cells in the probed volume, are rotationally disordered around the fibers axis (so-called "fiber-texture"), Characteristic peaks with uniaxial symmetry are also observed for probed volumes down to about $5*10^4$ unit cells[19], suggesting like-wise bulk-like properties. The radial, equatorial WAXS profile can be simulated by Gaussians for (hk0) peaks (Figure 1c). The two strongest peaks reflect density modulations within the β-sheets (210) and the inter-sheet stacking direction (020) reflection.

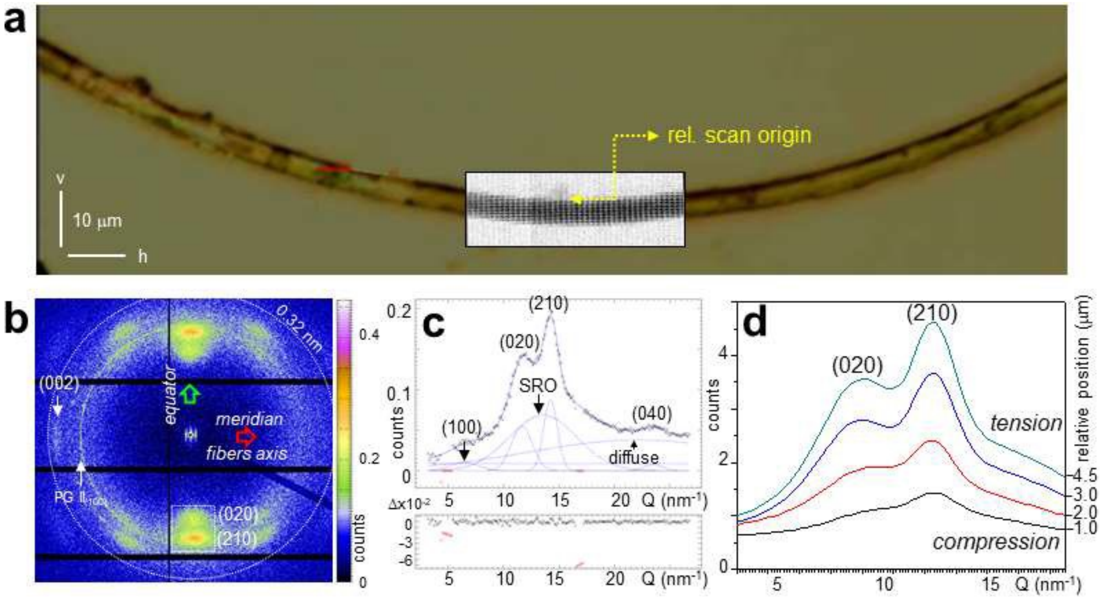

FIGURE 1 Scanning nanoXRD of bent thread in transmission geometry. a) View of thread along X-ray beam direction for r_b~231 µm; "h,v": horizontal and vertical scan-directions. The overlaid density map is based on pixels covering the (020)/(210) Bragg peaks. The relative origin of the 1D plot along the scanning direction normal to the fibers axis is placed at the first statistically significant pattern in the compression zone. b) Averaged pattern of unbent fiber (Figure S8g), indexed for β poly(L-alanine)[8] (see Figure S2) and polyglycine II (PG II) (100) reflection[18,19]. The rotational disorder of nanodomains around the fibers axis ("fiber texture") is at the origin of the silk reflections uniaxial symmetry. c) Equatorial intensity profile of b), fitted by Gaussians and 0-order polynomial ($Q=4\pi\sin\Theta\lambda^{-1}=2\pi/d$ with Θ: Bragg angle, λ: wavelength, d: lattice spacing). d) Equatorial intensity profiles of bent thread (r_b~231 µm) at selected radial positions from compression into tension zone. See Figure S9a for the relative position scale used.

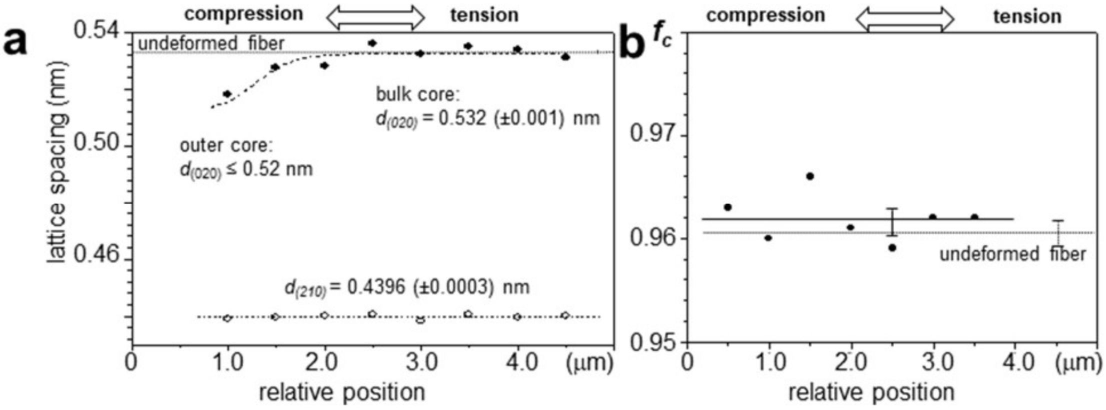

FIGURE 2 β-sheet nanodomains lattice metrics of bent thread (average of r_b: 446/231 µm). a) (020)/(210) lattice spacing (also called "*d*-spacing") variation across thread. Linear regression-line fit for (210) d-spacing; sigmoidal fit for the (020) *d*-spacing. Regression-line fit of $d_{(020)}$ variation for undeformed fiber (Figure S9b) is shown by a black, dotted line. b) Herman's orientation function (f_c) fitted by linear regression line (solid line). Regression-line fit of f_c variation for the undeformed fiber is indicated by a black, dotted line.

A broad Gaussian is attributed to "short-range order" (SRO) scattering from β-sheet nuclei. Indeed, MD simulations of MaSp1/MaSp2 secondary structures reveal small β-sheet stretches in the disordered domains capping the β-sheet cores[4].

The impact of bending on the nanodomains lattice is revealed by sharpening of the equatorial intensity profile from the compression to tension zone (Figure 1d). We attribute this to a difference in inter-sheet (020) and β-sheet (210) lattice spacing variation from compression to tension zone (Figure 2a). Indeed, the $d_{(210)}$ spacing of 0.4396 (±0.0003) nm for the bent thread does not depend on the position in the fiber and agrees to $d_{(210)}$=0.4397 (±0.0002) nm for the unbent fiber (Figure S9b). The $d_{(020)}$ spacing is reduced, however, by ~0.01 nm from about the middle of the thread to the edge of the compression zone (Figure 2a). The value of $d_{(020)}$=0.532 (±0.01) nm in bulk (Figure 2a) agrees to $d_{(020)}$=0.5328 (±0.0004) nm for the unbent fiber (Figure S9b). We derive a microstrain of $\varepsilon^{i}_{(020)}\sim -0.02$ at the interface in the compression zone from the inter-sheet $d_{(020)}$ spacing by $\varepsilon^{i}_{(020)} = [d^{i}_{(020)} - d^{unbent}_{(020)}] / d^{unbent}_{(020)}$ [20]. The reduction in $d_{(020)}$ spacing in the compression zone, while the $d_{(210)}$ is not affected, is attributed to weaker van der Waals forces between the peptide side-groups acting along the b-axis direction as compared to stronger hydrogen-bonding forces along the [210] direction (Figure S2). High-pressure XRD experiments of organic crystals with hydrogen-bonded sheets reveal also anisotropy in compressibility[21]. The observation that the $d_{(020)}$ lattice spacing reaches the value of the unbent fiber approximately in the middle of the bent fiber is expected for a neutral zone between compression and tension zones. The precision in $d_{(020)}$ determination is, however, not sufficient to localize the neutral zone, which could also be shifted towards the tension zone, as shown for bent carbon fibers[20]. The orientation distribution, expressed in terms of Herman's orientation function's f_c (Equation S1; *SupInf*), is not significantly modified by bending deformation (Figure 2b), suggesting that the level of microstrain has no significant effect on the local environment of nanodomains. Bending of the thread into a knot with an overall smaller bending radius results, however, in a strong increase in azimuthal width of equatorial peaks and increased diffuse scattering, suggesting disordering and size-reduction of nanodomains as well as a reduction in crystallinity (Figure S11a-c). Similar changes to fiber diffraction patterns are also observed for plastically deformed synthetic polymer fibers[22].

The meridional SAXS peak -also called "long period" (L_p) peak- (Figure 3c,d, S5a,b) has been attributed to periodic density modulations of crystalline and amorphous domains in nanofibrils (Figure 4a) forming a lamellar morphology[7]. The observation of usually only one meridional order (Figure 3c) suggests a thickness-distribution of crystalline β-sheets while highly ordered bagworm silk shows up to five orders[12]. By assuming cylindrical nanofibrils, a diameter of d_{cyl}^{NF}~7 nm was derived by Guinier-plot extrapolation of equatorial scattering[7,8]. A similar diameter of ~7.4 nm was observed by atomic force microscopy (AFM) for fibroin nanofibrils[23] and ~10 nm for spidroin nanofibrils of exfoliated *Trichonephila* dragline-type fibers[24]. Here, we assume for geometric modelling: d_{cyl}^{NF}~8 nm.

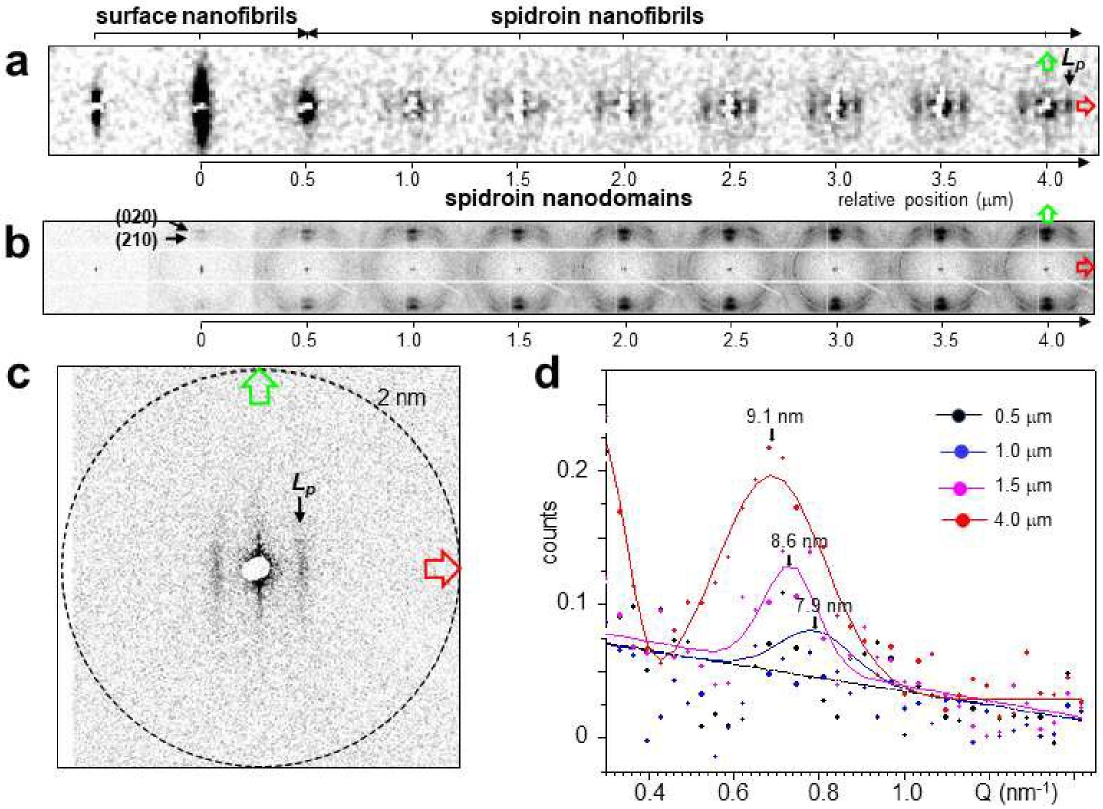

FIGURE 3 NanoXRD for unbent fiber. a) Evolution of SAXS patterns for radial scan of unbent fiber from surface to center. Each pattern corresponds to 20 patterns averaged along fiber axis. The relative origin (0) of the radial scan is placed at the maximum of the surface-layer's equatorial streak intensity. b) Corresponding evolution of WAXS patterns. c) SAXS pattern from 50 averaged pattern from the bulk of the fiber's core. d) Intensity evolution of meridional L_p peak in radial direction ($Q=2\pi/d$). Solid lines for 1.0/1.5/4.0 µm position correspond to Gaussian fits to the peak profiles (filled circles) with lattice spacing values for peak maxima. Black solid line corresponds to a 1st order polynomial fit for 0.5 µm position data.

The protein surface-layer attached to the spidroin core is revealed in unbent fibers by intensity-modulated equatorial scattering, which was simulated by cylindrical nanofibrils with a gradient in diameter of 40-150 nm, lacking, however, crystallinity[8]. Surface protein nanofibrils and core spidroin nanodomains co-exist at the center of the surface-layer Figure (3a,b) while core nanofibrils are only observed from about 1 µm distance from the surface-layer, in agreement with previous observations[8] (Figure 3d). The long period shows a gradual evolution of lamellar scattering from L_p~7.9 nm for nanofibrils nearest to the surface-layer to L_p ~9.1 nm in the bulk (Figure 3d). We assume therefore a surface-core transition zone with hindered nanodomains assembly into nanofibrils.

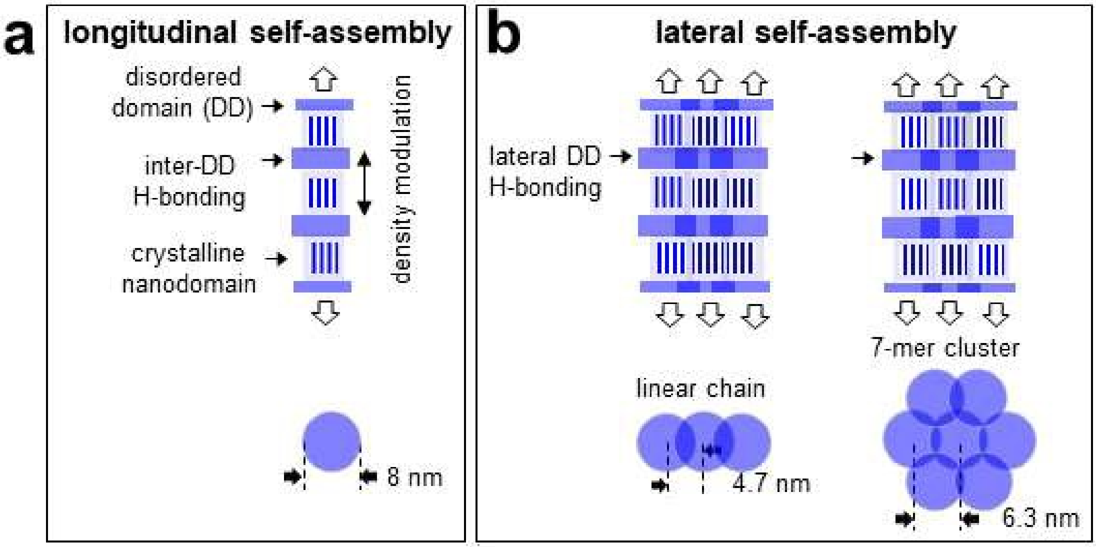

FIGURE 4 Schematic nanofibrillar assembly model. a) Above: side-view of nanofibrillar chain assuming monomer units composed of a crystalline β-sheets nanodomain, capped by disordered domains. The numbers of experimentally observed meridional orders depends on the length distribution of chain units (see text). Below: projection along nanofibrillar chain-axis assuming cylindrical shape with diameter d_{cyl}^{SNF} ~8 nm and homogeneous projection density. b) Lateral nanofibrillar assembly through H-bonding interactions of disordered domains into linear chains and 7-meric nanofibrils clusters. Experimental evidence for inter-nanofibrils distances related to these assemblies is discussed in the text.

2.2. Composite density map of bent fiber

The impact of bending deformation on spidroin nanofibrils assembly is revealed by changes to meridional and equatorial SAXS, such as absence of lamellar scattering in the DM, extending radially by ~2 µm from the outer interface into the core (Figure 5a,b), matching approximately the gradient in $d_{(020)}$ spacing (Figure 2a). The contours of this zone are defined by two lines of strong equatorial streaks running parallel to the fibers axis. The observation of lamellar scattering beyond this zone in the bulk suggests that the inner line corresponds to an interface between two core-shells. We attribute the streaks observed at the surface-core interface also to spidroin scattering. Indeed, diffuse, azimuthally broadened peaks centred at Q~1 nm^{-1} (d~6.3 nm) are observed in patterns from this interface (Figure 5b,c). These patterns are associated with even broader azimuthal (020)/(210) Bragg peak distributions, as $l \neq 0$ layer-line reflections (in particular (hk1); see Figure 1c) are contributing (Figure 5d, S6e,f). In view of the amorphous nature of surface proteins[8], we locate the origin of the diffuse peaks at the outer core's interface. In contrast, intensity modulated, narrow streaks are observed at the core-core interface (Figure 5e, S3a,b). These streaks are associated with WAXS patterns showing the same fiber texture peaks as bulk patterns from undeformed fibers (Figure 5f).

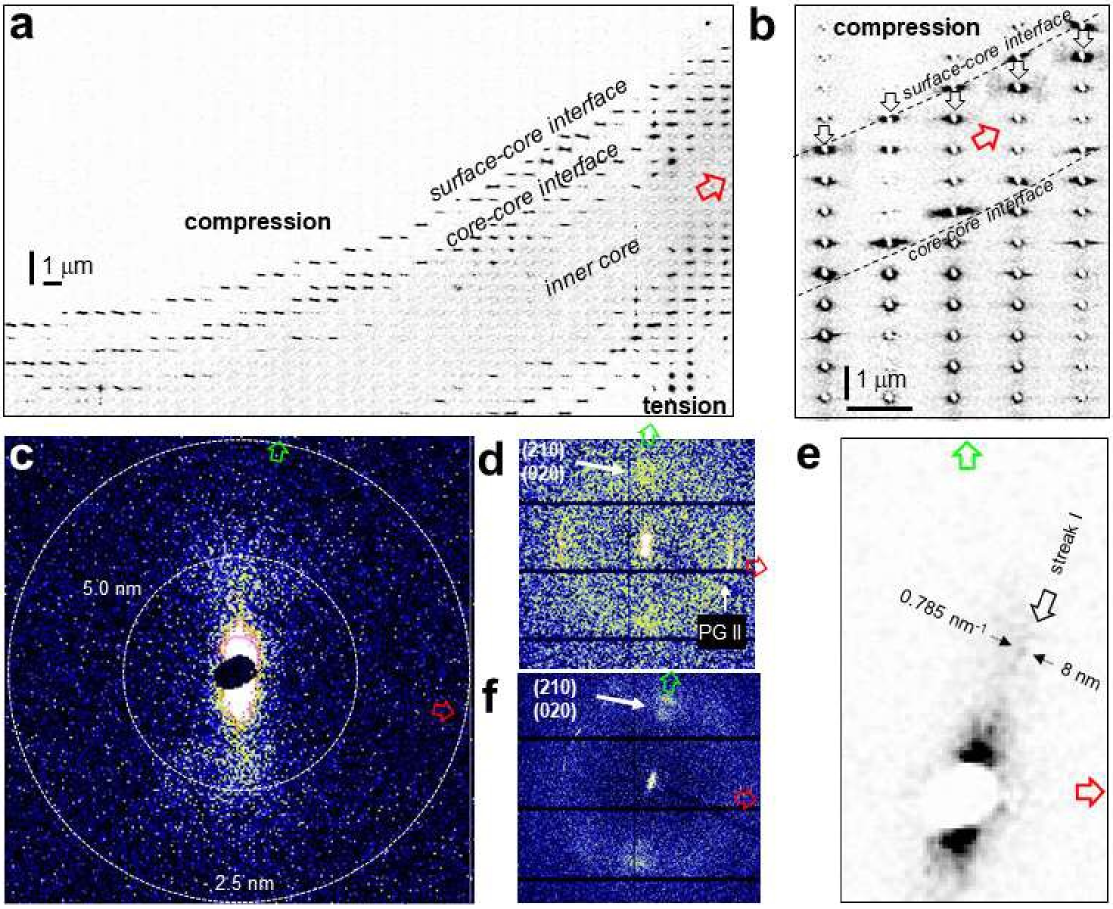

FIGURE 5 NanoXRD from bent thread: a) SAXS DM of r_b~446 μm fiber; 4x binned pixels covering $0.2<Q<1.6$ nm^{-1} range (red arrow: local fiber axis). b) Zoom of DM; contours of surface-core compression zone indicated by dashed line. Weak meridional, lamellar scattering is observed beyond a 2nd dashed line, attributed to a core-core interface. Black, open arrows depict patterns, at the surface-core interface, with broad equatorial diffuse scattering (patterns rotated by 90° from the macroscopic fiber axis; see *SupInf*). c) Average of five SAXS patterns showing broad diffuse scattering. d) WAXS range of pattern; 16x binned. **Core-core interface scattering:** e) Single SAXS pattern with modulated streak I in the centre of a broad, diffuse peak. f) Corresponding WAXS pattern.

2.3. Simulation of outer core-shell's interface

Simulations were based on the azimuthally averaged profile of an average of 5 patterns containing the diffuse peak (Figure 5c, S3a). To emphasize weaker features at higher Q-values we chose a 1D Kratky plot display[25]: I(Q)*Q^2 versus Q (Figure 6a). The plot can be roughly separated into a lower-Q branch up to a broad, diffuse peak and a higher-Q branch covering the diffuse peak. The lower-Q branch shows smeared, weak modulations, while the higher Q-branch shows a series of well-defined peaks (Figure 6a,b).

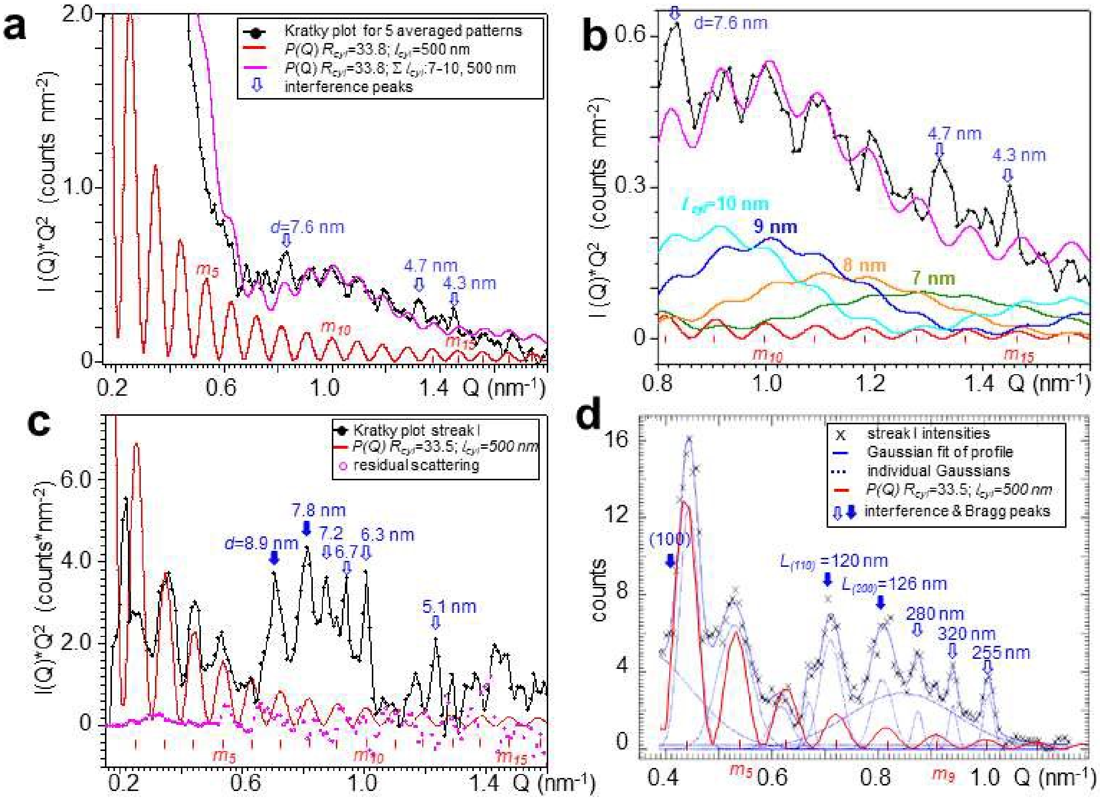

FIGURE 6 Experimental and simulated interface profiles. Surface-core interface: a) 1D Kratky plot[25] of diffuse SAXS (black line and circles; see Figure S3a for azimuthal averaging of 2D pattern). Simulated plot (red and pink lines; see legend for simulation parameters) and peaks attributed to interference (blue, open arrows). Positions of the maxima (m_i) of the simulated red curve are indicated by red bars (1st maximum: m_1). Pink line: scaled sum of *P(Q)* values for cylinder length l_{cyl}: 7,8,9,10 and 500 nm. b) Zoom into a) and individual l_{cyl} contributions to simulated profile (Figure S13d). **Core-core interface:** c) Kratky plot of streak I in Figure 5e (black circles and line). Simulated cylindrical form factor scattering in red, scaled at m_3 to experimental curve; simulation parameters are shown in legend. Pink circles: residual scattering at 90^0 to streak I. For statistical analysis of residual scattering see Figure S5a. d) Intensity profile of streak I fitted by Gaussians and 0-order polynomial. "x": experimental data. Blue dotted peaks: individual Gaussians fitted to form factor, interference peaks and diffuse background modulation. Blue solid line through experimental points: sum of fitted Gaussian and 0-order polynomial. Red solid line: simulated form factor for parameters shown in legend. Open, blue arrows in c/d: position of interference peaks. Solid blue arrows: Miller's indices for hexagonal lattice: $a=b=17.8$ nm, $\gamma=120^0$. *d*-spacing and particle size (*L*) values were derived from the width of Gaussian profiles.

The positions of the narrow peaks in the higher-Q branch agree to form factor scattering *P(Q)* from homogeneous cylinder-like shapes (Equation S2 and *SupInf*) of radius R_{cyl} =33.8 nm[8,9]. The modulated profile including diffuse peak can be simulated by short cylinders $l_{cyl} << R_{cyl} \sim L_p$ (S12a,b) with a length distribution of 7 nm$< l_{cyl} <$10 nm for Δl_{cyl} increments of 1 nm. The simulated profile matches up to about 13 modulations (m_{13}) in the Kratky plot and reproduces the smearing of form factor peaks in the lower-Q branch (Figure 6a,b; S12c,d). Several peaks, which do not match the simulated curve, are attributed to lateral interferences between neighbouring nanofibrils. Such peaks have also been identified for scattering from meso-scale nanofibrillar bundles in bagworm silk[9]. Indeed, a 4.7 nm peak (Q=1.35 nm^{-1}) -located between the m_{14}/m_{15} maxima- is attributed to lateral nanofibrils assembly (Figure 4b). The 4.7 nm inter-chain distance implies significant interpenetration with H-bonding interactions of disordered domains (Figure 4b). We exclude lateral assembly via β-sheet nanodomains as aggregates of crystalline nanodomains have not been observed for dragline-type fibers by nanoXRD[8,19,26] nor for *B. mori* fibers by low voltage transmission electron microscopy (LV-TEM)[27]. A 4.3 nm peak (Q=1.45 nm^{-1}), differing slightly from the m_{15} maximum is attributed to a modulated inter-chain distance[9]. A ~7.6 nm peak (Q~0.83 nm^{-1}) is slightly outside the m_8 position (open blue arrow in Figure 6a) but within the range of interference peaks from the inner core's interface (Figure 6c and text).

2.3. Simulation of core-core interface

Simulations were performed for two distinct modulated streaks observed in single patterns, which are better defined than for the outer core's interface (Figure 5e, S3a,b). The streaks are tilted by 10-20° against the equatorial axis, suggesting twisting of bundles along the fibers axis. We assume that the streaks represent characteristic structural features, as other streaks show a mixture of scattering features from the two streaks.

The Kratky profile of streak I (Figure 5e) can also be approximately separated into lower-Q branch and a higher-Q branch with a series of narrow peaks, overlaying a broad diffuse peak (Figure 6c,d). The narrow peaks are generally better-defined than for the outer core-interface (Figure 6a,b). We simulated the peaks in the lower Q-branch by *P(Q)* scattering (*SupInf*: Equation S2) for homogeneous cylindrical shapes with R_{cyl}=33.5 nm and $l_{cyl} >> R_{cyl}$=500 nm (Figure 6d). *P(Q)* peaks can be identified up to the m_6 maximum (Q~0.6 nm^{-1}). The simulated profile becomes weak with respect to the higher-Q peaks, which can be distinguished from residual fluctuations up to at least Q_{max}~1 nm^{-1} (~6.3 nm) (Figure 6a, S4a). These peaks are too strong for a model of short meso-scale cylinders applied to the outer core-interface. We rather assume interferences from two discrete structural features, corresponding to particle sizes of ~120 nm and >250 nm, which can be related to domain sizes (Figure 6b).

The two peaks corresponding to the smaller particle size are attributed to a structure factor -*S(Q)*- term (*SupInf*). They agree to (110)/(200) reflections of a hexagonal lattice with unit cell parameters: *a*=*b*=17.8 nm; γ=120^0 (Figure 7a, S13a). Particles with a circular projection cross-section of ~18 nm diameter resemble globular particles observed by AFM in silks[28,29]. Analysis was based on the model of 7-meric nanofibril clusters with d_{cyl}^{SNF} ~8 nm (see above), stabilized by H-bonding interactions. Indeed, a ~18 nm circular cross-section covers the outer dimension of a cluster composed of central nanofibril with a hexagonal shell of six nanofibrils (Figure 4b,7a,b). The remaining peaks corresponding to larger particle sizes (Figure 6d) are attributed to inter-nanofibrillar interferences. Indeed, the 6.3 nm interference peak (Figure 6c) agrees to the distance of the central nanofibril to the shell nanofibrils while the distance of nanofibrils in neighbouring shells of ~5.2 nm is slightly larger than the linear chain separation of 4.7 nm (Figure 4b). A weak peak with 5.1 nm spacing (Q=1.2 nm^{-1}) is tentatively attributed to interferences from nanofibrils in neighbouring direct shells (Figure 6c). Each cluster is surrounded by a secondary shell of 6 clusters through 6 bridges of two direct-shell nanofibrils (Figure 7a,b). Such clusters represent an intermediate assembly level with respect to meso-scale bundles. The absence of observable Bragg peaks with higher Q-values than the (200) reflection suggests that the clusters projection density lacks internal structure resulting in reciprocal space modulations. We tested the clusters model by calculating discrete structure factor amplitudes: $F_{(hk0)}^2$ (*SupInf,* Equation S3), assuming *P6* hexagonal space group symmetry[30], with the central nanofibril of the cluster occupying the origin of the unit cell and one of the shell's nanofibrils located on the a-axis (Figure 7a, S13a). The positions of the other nanofibrils in the unit cell are generated by symmetry operations (for details see: *Supp Inf*). The model suggests hydrogen-bonding pathways between neighbouring clusters (Figure 7b). An interference peak corresponding to the distance of ~6.3 nm of the central nanofibril to its direct shell is not allowed for the *P6* space group. The observed peak suggests therefore a 2nd type of domains without 2D hexagonal packing, which is supported by larger domain sizes derived by Scherrer's equation from the 6.3 nm peak width (Figure 6d). This is also the case for other interference peaks observed up to Q~1.0 nm^{-1}, which match near-neighbour nanofibril interferences along H-bonding pathways (Figure 7b).

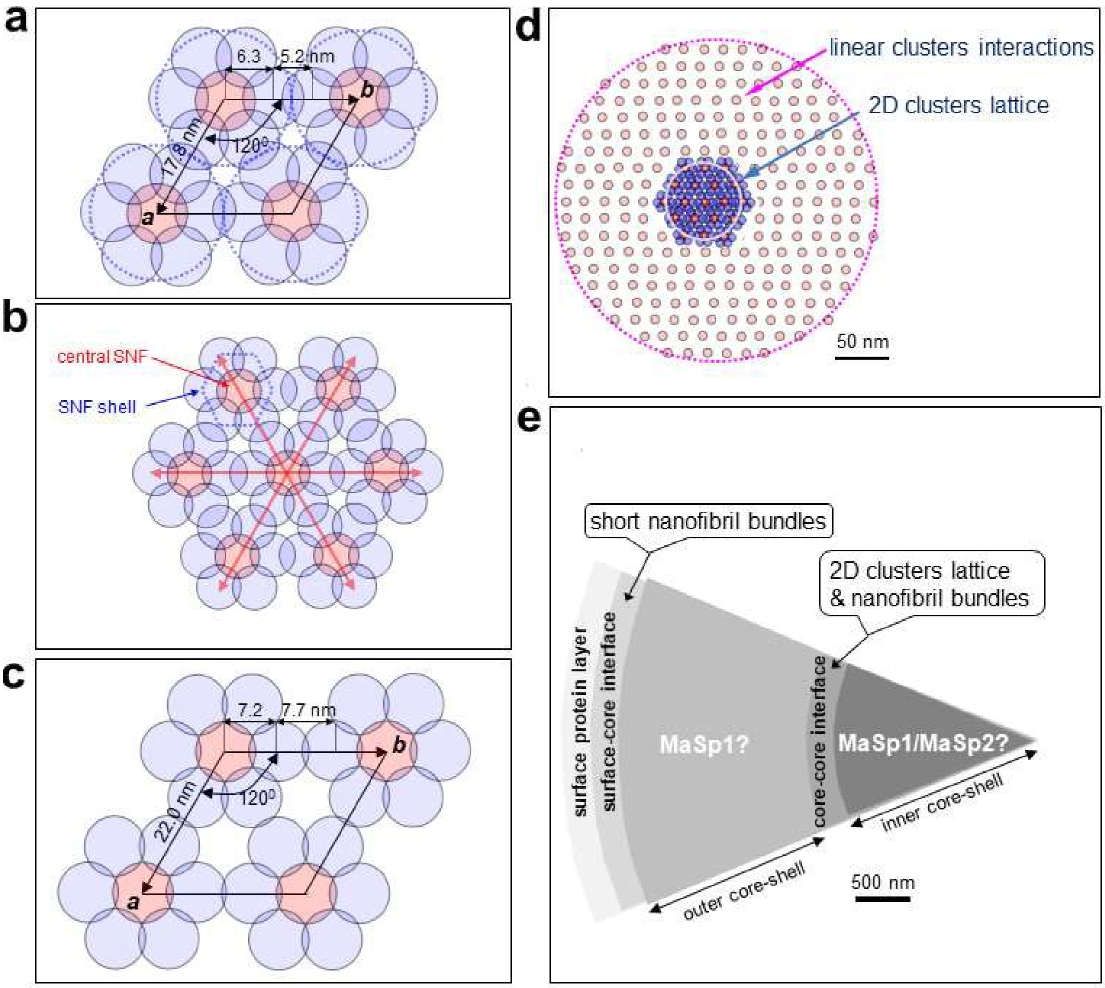

FIGURE 7 Proposed structural models for nanofibril assembly into clusters at the core-core interface. a) Model of hexagonal lattice based on clusters of 7 nanofibrils occupying two different sites (Figure S4a) with intra- and inter-bundle H-bonding interactions, assuming d_{cyl}^{SNF}=8 nm. The central nanofibril of each cluster is depicted in red and the shell nanofibrils in blue (see *SupInf*). The projection contours of a densest packing of 17.8 nm diameter cylindrical particles are schematically indicated by dotted blue circles. b) Hexagonal super-cluster with enhanced hydrogen-bonding pathway directions indicated by red arrows. c) Schematic display of hexagonal lattice with increased a/b parameters resulting in weaker H-bonding interactions. d) Schematic model of proposed meso-scale hierarchical organization at core-core interface. The contours of meso-scale hexagonal clusters lattice and clusters lattice with linear interactions are shown by blue and pink circles. The positions of central nanofibrils of isolated clusters are shown as red circles. Full clusters are only shown for the hexagonal lattice e) proposed schematic shell-model for fibers cross-section and structural features derived by SAXS for a bent fiber. The hypothetical MaSp1 and MaSp2 distribution shown is based on spidroin-specific imaging of *Nephila* dragline fibers[31].

The lattice shown in Figure 7a,b is attributed to the highest state of compaction at the core-core interface. Indeed, analysis of a slightly different 2nd streak (streak II) from the core-core interface (Figure S4b) suggests a lattice of clusters with enlarged dimensions corresponding to less compaction (Figure S4b). The corresponding Kratky curve shows also two branches but no broad diffuse peak in the Q-range observed for streak I (Figure S15a). The lower-Q branch peaks agree also to $P(Q)$ scattering from meso-scale cylinders of R_{cyl}=33.5 nm and l_{cyl}=500 nm while the higher Q-branch can be simulated by $F_{(hk0)}$ peaks for a hexagonal lattice with enlarged unit-cell of a=b=22.0 nm; γ=120^0 (Figure 7c, S14b,c). We attribute a 7.7 nm peak to the inter-nanofibril distance of neighbouring shells (see discussion in *SupInf*), implying a distance of 7.2 nm from the central nanofibril to its direct shell. The increase of the inter-nanofibril distance by ~0.9 nm is attributed to an increasing distance of the clusters from the interface, resulting in reduced compression.

The presence of cluster lattice domains with less compaction suggests a fraction of isolated clusters, possibly extending into the bulk. Diffuse scattering underlying interference and form factor peaks -simulated in Figure 6d by two broad Gaussians with d~17.9 nm (Q~0.35 nm^{-1}) and d~7.4 nm (Q~0.85 nm^{-1})- provides support for this hypothesis. Indeed, one could model the ~7.4 nm Gaussian by $P(Q)$ for spherical or short cylindrical shapes with diameters of 13-14 nm, corresponding roughly to the dimension of rotationally disordered 7-meric nanofibril clusters (Figure 7a,c). The model generates, however, too much intensity for the tails of the Guinier range[25], corresponding to the diffuse scattering covered by the ~17.9 nm Gaussian. We show in Figure S14c,d that the range of diffuse scattering can be better modelled by a mixture of $P(Q)/S(Q)$ scattering, based on stacked disks[32] of 13 nm diameter with a ~5.5 nm thick core and a ~1 nm skin-layer of lower density (*SupInf*). Such core/shell particles could be due to spidroin molecules from the outer core-shell as the ~7.5 nm density modulation of the stacked disks corresponds to the spacing of the emerging meridional L_p peak close to the surface-layer (Figure 3c) and the azimuthal width of the diffuse peak (Figure S4d) resembles diffuse scattering from the outer core-shell's interface (Figure 5c, S2c).

3. Conclusions

Our results reveal that meso-scale order exists in both dragline-type and silkworm-type fibers[9,12,33] *R*adial fibers show, however, a more complex hierarchical organization at core-surface layer and core-core interfaces while meso-scale nanofibrillar bundles are for silkworm-type fibers only present at the core-surface layer interface. Indeed, short length meso-scale nanofibrillar bundles at the core-surface interface of radial fibers suggest hindered axial spidroin nanofibrils assembly in the presence of surface proteins. This is supported by the absence of a lamellar morphology in the vicinity of surface-layer for undeformed fibers, suggesting that the outer core-shell contributes rather to fibers elasticity. An important function of the interaction of outer core-shell's spidroin with surface-layer proteins could be keeping the multi-layered skin[13] attached to the core. The tight association requires in practice mechanical disruptive processes, such as freeze-thaw cycles, for separating the surface-layers from the core[13]. The spatial resolution of the present study does, however, not exclude a finer structuring of the surface-core interface.

The core-core interface shows a mixture of extended length meso-scale nanofibrillar bundles and nanofibrillar clusters forming 2D lattice domains, which were not observed for silkworm-type fibers. There is preliminary evidence for a fraction of isolated clusters at the core-core interface, which could increase with radial distance from the surface. A more detailed study of the distribution of such features will, however, require probing sections as for bagworm silk[9]. The densification of an inner-core interface supports the two core-shell model based on a heterogeneous spidroin distribution observed for *Nephila* dragline[13,31]. Indeed, spidroin-specific imaging reveals homogeneous MaSp1 distribution across the core while MaSp2 was found populating only an inner core-shell. It is therefore tempting speculating that nanofibrillar clusters are composed of a central MaSp2 nanofibril, which is hydrogen-bonded to a MaSp1 nanofibrils shell but random MaSp1/MaSp2 replacement cannot be excluded. Caution is, however, necessary when comparing spidroin-specific imaging obtained from ultrathin cross-sections with bulk-type volumes probed by nanoXRD. Indeed, spidroin-specific imaging[31] does not reveal evidence for spidroin densification at interfaces observed in the present study. The hypothesis that "MaSp2 is restricted to the amorphous fraction of the matrix contributing to the elasticity of the fiber while MaSp1 resides predominantly in the crystalline areas"[31], is also not supported by nanoXRD studies. Indeed, no evidence for a variation in crystallinity across *Argiope* radial fibers was observed in the present or related studies[8,19]. Local MaSp2 aggregates observed by imaging at the center of the cross-sections[31] were also not observed in the SAXS-range, although aggregates can be observed for thermally degraded, ultrathin protein films[34].

The dimensions of nanofibrils and bundles scale discussed in this study scale well to AFM results. Indeed, loosely connected globules with 6.5-20.5 nm size distribution in *Argiope* dragline-type silk were attributed to spidroins nonperiodic lattice (NPL) model[29]. Globular features of 20-30 nm in silkworm and *Nephila's* MA silk were attributed to the diameter of twisted nanofibrils composed of β-sheet nanodomains and disordered chains[35,36].

4. Experimental Section

Samples and supports: The collection of anchor-thread silk from *A. bruennichi's* orb-web has been described elsewhere[8]. Single threads were deposited on X-ray transparent Si_3N_4 membranes. For details see *SupInf.*

Synchrotron radiation experiments: were performed at the ID13 beamline[8] of the ESRF-EBS (Extremely Brilliant Source)[37]. A monochromatic beam of $\lambda = 0.0835$ nm was focused to a $\sim 190_{hor} x 170_{vert}$ nm full-width-half-maximum (fwhm) spot at the sample position with a flux of $\sim 5*10^9$ photons/s. Samples were probed in transmission geometry by step-scanning through the focal spot. At each scan-position a two-dimensional (2D) diffraction pattern was recorded by a silicon pixel detector[8,19]. Mesh-scans correspond to a sequence of vertical line-scans, equidistant along the horizontal axis. We used 500 nm step-increments normal and 1000 nm along the fiber's axis for exposure times of -typically- 3 s/pattern.

Acknowledgment

We thank the ID13 beamline responsible -M. Burghammer- for provision of in-house research beamtime and the ID13 beamline scientist M. Rosenthal for providing support during the experimental period.

Funding

The authors acknowledge that no external funding was received in support of this research.

Author Contributions

C.R. conceived the research, collected the samples, designed the experiments and analyzed the data. T.G. collected the SR data. C.R. wrote the paper with input by T.G.

Conflict of Interest

The authors declare that they have no competing interests.

Data and Materials Availability

All data needed to evaluate the conclusions in the paper are present in the paper and/or the Supplementary Material. Additional data related to this paper may be requested from the authors.

Supporting Information

is available at .... The file contains detailed information on materials, methods, data reduction, data analysis and complementary results.

References

1 Foelix, R. F. *Biology of Spiders*. (Oxford University Press, 2011).

2 Gosline, J. M., DeMont, M. E. & Denny, M. W. The Structure and Properties of Spider Silk. *Endeavour* **10**, 37-43 (1986).

3 Malay, A. D., Craig, H. C., Chen, J., Oktaviani, N. A. & Numata, K. Complexity of Spider Dragline Silk. *Biomacromolecules* **23**, 1827-1840 (2022).

4 Keten, S. & Buehler, M. J. Nanostructure and Molecular Mechanics of Spider Dragline Silk Protein Assemblies. *J. R. Soc. Interface* **7**, 1709-1721 (2010).

5 Grubb, D. T. & Jelinski, L. W. Fiber Morphology of Spider Silk: The Effects of Tensile Deformation. *Macromolecules* **30**, 2860-2867 (1997).

6 Riekel, C., Burghammer, M. & Rosenthal, M. Mesoscale Structures in Amorphous Silks from a Spider's Orb-Web. *Sci. Rep.* **10**, 18205, doi:10.1038/s41598-020-74638-0 (2020).

7 Yang, Z., Grubb, D. T. & Jelinski, L. W. Small-Angle X-ray Scattering of Spider Dragline Silk. *Macromolecules* **30**, 8254 - 8261 (1997).

8 Riekel, C., Burghammer, M., Ferrero, C., Dane, T. & Rosenthal, M. Nanoscale Structural Features in Major Ampullate Spider Silk. *Biomacromolecules* **18**, 231-241 (2017).

9 Yoshioka, T., Kameda, T., Burghammer, M. & Riekel, C. Mesoscale Confinement in Bagworm Silk: A Hidden Structural Organization. *Nano Lett.* **23**, 757-764 (2023).

10 Cetinkaya, M., Xiao, S., Markert, B., Stacklies, W. & Graeter, F. Silk Fiber Mechanics from Multiscale Force Distribution Analysis. *Biophys. J.* **100**, 1298–1305 (2011).

11 Giesa, T., Arslan, M., Pugno, N. M. & Buehler, M. J. Nanoconfinement of Spider Silk Fibrils begets Superior Strength, Extensibility and Toughness. *Nano Lett.* **11**, 5038-5046 (2011).

12 Yoshioka, T., Tsubota, T., Tashiro, K., Jouraku, A. & Kameda, T. A Study of the Extraordinarily Strong and Tough Silk Produced by Bagworms. *Nat Comm* **10**, 1469 (2019).

13 Sponner, A. *et al.* Composition and Hierarchical Organisation of a Spider Silk. *PLOS One* **10**, e998 (2007).

14 Keten, S., Xu, Z., Ihle, B. & Buehler, M. J. Nanoconfinement Controls Stiffness, Strength and Mechanical Toughness of β-Sheet Crystals in Silk. *Nat Mater* **9**, 359-367 (2010).

15 Blackledge, T. A., Kuntner, M. & Agnarsson, I. The Form and Function of Spider Orb Webs: Evolution from Silk to Ecosystems. *Adv. Insect Phys.* **41**, 175-262 (2011).

16 Work, R. W. & Emerson, P. D. An Apparatus and Technique for the Forcible Silking of Spiders. *J. Arachnol.* **10**, 1-10 (1982).

17 Marsh, R. E., Corey, R. B. & L.Pauling. The Structure of Tussah Silk Fibroin. *Acta Cryst.* **8**, 710-715 (1955).

18 Crick, F. H. C. & Rich, A. Structure of Polyglycine II. *Nature* **176**, 780-781 (1955).

19 Riekel, C., Burghammer, M. & Rosenthal, M. Nanoscale X-Ray Diffraction of Silk Fibers. *Frontiers in Materials* **6**, 315 (2019).

20 Loidl, D., Paris, O., Burghammer, M., Riekel, C. & Peterlik, H. Direct Observation of Nanocrystallite Buckling in Carbon Fibers under Bending Loadn. *PRL* **95**, 225501-225504 (2005).

21 Katrusiak, A. High-Pressure X-ray Diffraction Study of Pentaerythritol. *Acta. Cryst.* **B51**, 837-879 (1995).

22 Riekel, C., García-Gutiérrez, M. C., Gourrier, A. & Roth, S. Recent Synchrotron Radiation Microdiffraction Experiments on Polymer and Biopolymer Fibers. *Anal and Bioanal Chem* **376**, 594-601 (2003).

23 Eliaz, D. *et al.* Micro and Nano-Scale Compartments Guide the Structural Transition of Silk Protein Monomers into Silk Fibers. *Nat Comm* **13**, 7856 (2022).

24 Perera, D., Li, L., Walsh, C., Wang, Q. & Schniepp, H. C. Natural Spider Silk Nanofibrils Produced by Assembling Molecules or Disassembling Fibers. *Acta Biomater.* **168**, 323-332 (2023).

25 Glatter, O. & Kratky, O. in *Small Angle X-ray Scattering* (eds O. Glatter & O. Kratky) (Academic Press, 1982).

26 Sampath, S. *et al.* X-Ray Diffraction Study of Nanocrystalline and Amorphous Structure within Major and Minor Ampullate Dragline Spider Silks. *Soft Matter* **8**, 6713-6722 (2012).

27 Drummy, L. F., Farmer, B. L. & Naik, R. R. Correlation of the β-Sheet Crystal Size in Silk Fibers with the Protein Aminoacid Sequence. *Soft Matter* **3**, 877-882 (2007).

28 Du, N. *et al.* Design of Superior Spider Silk: From Nanostructure to Mechanical Properties. *Biophys J* **91**, 4528–4535 (2006).

29 Perez-Rigueiro, J., Elices, M., Plaza, G. R. & Guinea, G. V. Similarities and Differences in the Supramolecular Organization of Silkworm and Spider Silk. *Macromolecules* **40**, 5360-5365 (2007).

30 Arayo, M. I. Vol. International Tables for X-ray Crystallography A (International Union of Crystallography, 2016).

31 Sponner, A., Unger, E., Grosse, F. & Weisshart, K. Differential Polymerization of the Two Main Protein Components of Dragline Silk during Fibre Spinning. *Nature Materials* **4**, 772-775 (2005).

32 Kratky, O. & Porod, G. Diffuse Small-Angle Scattering of X-Rays in Colloid Systems. *J. Colloid Science* **4**, 35-70 (1949).

33 Yoshioka, T. & Kameda, T. Hexagonal Packing of Nanofibrils in *Bombyx mori* Silkworm Silk Revealed by Small-angle X-ray Scattering Analysis. *J. Silk Sci. Tech. Jpn.* **28**, 129-135 (2020).

34 Pechkova, E., Nicolini, C., Burghammer, M. & Riekel, C. Emergence of Amyloidic Fibrillation in 2D-ordered Langmuir-Blodgett Protein Multilayers upon Heating. *APL* **117**, 053701 (2020).

35 Xu, G., Gong, L., Yang, Z. & Liu, X. Y. What makes Spider Silk Fibers So Strong? From Molecular-Crystallite Network to Hierarchical Network Structures. *Soft Matter* **10**, 2116 (2014).

36 Du, N., Yang, Z., Liu, X. Y., Li, Y. & Xu, H. Y. Structural Origin of the Strain-Hardening of Spider Silk. *Adv. Funct. Mater.* **21**, 772-778 (2011).

37 Dimper, R. *et al.* *Orange Book: ESRF Upgrade Programme Phase II (2015-2022)-Technical Design Study* (ESRF, The European Synchrotron., 2015).